An Ultrahigh Responsivity (9.7 mA W^{-1}) Self-Powered Solar-Blind Photodetector Based on Individual ZnO–Ga_2O_3 Heterostructures

*Bin Zhao, Fei Wang, Hongyu Chen, Lingxia Zheng, Longxing Su, Dongxu Zhao, and Xiaosheng Fang**

Highly crystallized ZnO–Ga_2O_3 core–shell heterostructure microwire is synthesized by a simple one-step chemical vapor deposition method, and constructed into a self-powered solar-blind (200–280 nm) photodetector with a sharp cutoff wavelength at 266 nm. The device shows an ultrahigh responsivity (9.7 mA W^{-1}) at 251 nm with a high UV/visible rejection ratio ($R_{251\ nm}/R_{400\ nm}$) of 6.9×10^2 under zero bias. The self-powered device has a fast response speed with rise time shorter than 100 μs and decay time of 900 μs, respectively. The ultrahigh responsivity, high UV/visible rejection ratio, and fast response speed make it highly suitable in practical self-powered solar-blind detection. Additinoally, this microstructure heterojunction design method would provide a new approach to realize the high-performance self-powered photodetectors.

1. Introduction

When solar radiation goes through the Earth's atmosphere, the waveband of 200–280 nm (solar-blind range) cannot arrive the Earth's surface due to the absorption of ozone and vapors.[1,2] Solar-blind photodetectors, for a "black background" on the earth, have many civil and military applications including the missile warning, fire alarms, and environmental monitoring by transforming ultraviolet (UV) radiation signals into electrical energy directly.[1–6] Recently, a large variety of wide bandgap semiconductors are investigated to design solar-blind photodetectors, such as $Al_xGa_{1-x}N$, $Zn_xMg_{1-x}O$, diamond, and the monoclinic gallium oxide (β-Ga_2O_3).[7–15] The alloy materials $Al_xGa_{1-x}N$ and $Zn_xMg_{1-x}O$, with high Al and Mg composition, respectively, can achieve solar-blind photodetection, but the crystal quality of $Al_xGa_{1-x}N$ films deteriorates rapidly and the $Zn_xMg_{1-x}O$ appears phase segregation.[7–11,15] The diamond has a large indirect band gap (≈5.5 eV), which shows a low quantum efficiency and limits its detection wavelength to shorter than 225 nm.[12,13]

In particularly, β-Ga_2O_3 is an excellent candidate for solar-blind photodetection with a direct wide band gap of ≈4.9 eV (253 nm).[15] Owing to the single crystal and high internal gains of nanostructured photodetector, different kinds of β-Ga_2O_3 nanostructure based photodetectors have been developed.[14,16–18] Nevertheless, most β-Ga_2O_3 nanostructured detectors are photoconductive type with relatively slow response speed (approximately in seconds) due to the persistent photoconductivity effect. In addition, an external energy supply is usually required to obtain a desirable responsivity, which not only greatly increase the device size and energy consumption but also largely limit their long-term application in some unmanned hazardous atmosphere or harsh environment. Thus, high performance self-powered photodetectors operating without an external power source exhibit huge advantages.[19–22]

Generally, the self-powered photodetectors are achieved by traditional photovoltaic effect by means of Schottky junctions, p–n junctions, and heterojunctions.[23,24] Self-powered solar-blind photodetector based on Au/β-Ga_2O_3 Schottky junction was successfully fabricated.[25] However, because of the very weak solar-blind wavelength signals, the responsivity of such solar-blind photodetectors is still lower than expected. While for β-Ga_2O_3 material, as an intrinsic n-type semiconductor, it is difficult to realize p-type doping of β-Ga_2O_3, and few reports on β-Ga_2O_3 homojunction devices can be found.[26,27] Therefore, β-Ga_2O_3 based heterojunction devices turn out to be an alternative. To date, heterojunctions based on SiC/β-Ga_2O_3 film and Ga_2O_3/SnO_2 core–shell nanowire structures have been reported to construct solar-blind photodetectors, but they always require an external power source as the driving force to generate photocurrent.[27,28] To fabricate solar-blind photodetectors with high performance, the ability of constructing heterojunction with high crystal quality and lattice matching of two different materials are very important. ZnO, with a very small lattice mismatch (<5%) with Ga_2O_3, is a good candidate to construct heterostructure with Ga_2O_3, and Ga_2O_3/ZnO nanowire

Dr. B. Zhao, Dr. H. Y. Chen, Dr. L. X. Zheng, Dr. L. X. Su, Prof. X. S. Fang
Department of Materials Science
Fudan University
Shanghai 200433, P. R. China
E-mail: xshfang@fudan.edu.cn
Dr. F. Wang, Prof. D. X. Zhao
State Key Laboratory of Luminescence and Applications
Changchun Institute of Optics
Fine Mechanics and Physics
Chinese Academy of Sciences
Changchun 130033, P. R. China

DOI: 10.1002/adfm.201700264

composites with a core–shell geometry have been synthesized using a two-step chemical vapor deposition (CVD) method, but a mass of defects in the grain boundaries between the two materials limit their application in photodetectors.[29] Hence, as the crystal quality of the composite film, grain boundary between two different materials as well as the nanoscale size play a vital role, it is still a big challenge to achieve high performance (especially high responsivity) self-powered solar-blind β-Ga_2O_3-based photodetectors. In our previous study, highly crystallized ZnO–Ga_2O_3 core–shell heterostructure microwires were synthesized following a simple one-step CVD method, which showed few noticeable structural defects at the interface between the materials, and high performance solar-blind avalanche photodetector was realized based on this ZnO–Ga_2O_3 microstructure heterojunction.[30]

Herein, the growth mechanism of the highly crystallized ZnO–Ga_2O_3 heterostructure microwires has not only been further analyzed and discussed, but also high-performance self-powered solar-blind photodetector device has been fabricated based on an individual ZnO–Ga_2O_3 microwire, which shows a sharp cutoff edge at the wavelength of 266 nm. The experimental results in this work reveal that the heterojunction device based on single microstructure could function with high performance in terms of high responsivity, high UV/visible rejection ratio and fast response speed under zero bias. In addition, to get more insight into the working mechanism of the self-powered mode, the back-to-back junction configuration device and the energy band diagram are carefully investigated. This high-performance self-powered solar-blind photodetector has high potential applications in insecure communication and space detection.

2. Results and Discussion

Figure 1a shows the photograph of the as-synthesized ZnO–Ga_2O_3 core–shell microwires by a one-step CVD process revealing a mass of microwires grown on the Si substrate with ZnO film as the seed layer. The scanning electron microscopy (SEM) image of the core–shell microwire indicates that the average diameter is about 10 µm as shown in Figure 1b. The cross sectional SEM image (inset of Figure 1b) indicates that the cross section of the ZnO–Ga_2O_3 core–shell microwire is quadrangular. Figure 1c,d shows the structural morphology of the as-synthesized ZnO microwire and Ga_2O_3 microbelt, respectively. The inset of Figure 1c indicates that the cross section of the pristine ZnO microwire is also a quadrangle shape, similarly to that of the ZnO–Ga_2O_3 microwire. While the Ga_2O_3 is a wide belt structure (inset of Figure 1d). A low-magnification transmission electron microscopy (TEM) image of the cross-sectional slice of the ZnO–Ga_2O_3 microwire prepared using focused ion beam etching is shown in Figure S1 (Supporting Information), demonstrating a distinguished core–shell heterostructure. The high resolution TEM (HR-TEM) image (Figure 1e) reveals that the lattice spacing of the ZnO core and the Ga_2O_3 shell is 0.26 and 0.47 nm, respectively, and the lattice interface between these two materials is homogeneous and atomically sharp with few noticeable structural defects. By contrast, the ZnO–Ga_2O_3 microwire synthesized using a two-step CVD method is shown in Figure S2 (Supporting Information), which demonstrates that the interface between the two materials is obvious discontinuous with a boundary. The HR-TEM image of the core (Figure 1f) illustrates the lattice spacing of 0.26 nm corresponding to the separation of (0 0 2) planes of the hexagonal ZnO. The HR-TEM image of the shell (Figure 1g) demonstrates the lattice spacing of 0.47 nm corresponding to ($\bar{2}$ 0 1) plane separations of the monoclinic β-Ga_2O_3. The

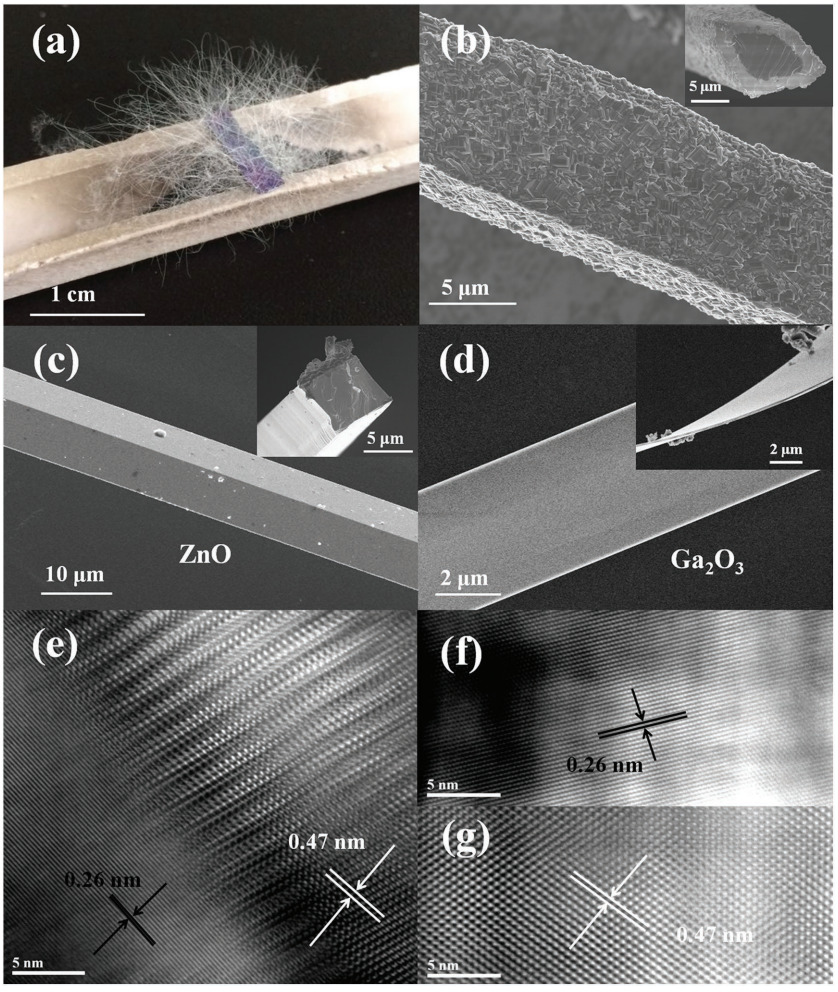

Figure 1. a) The photograph of the as-synthesized ZnO–Ga_2O_3 core–shell microwires. b–d) The SEM images of single ZnO–Ga_2O_3 core–shell microwire, ZnO microwire and Ga_2O_3 microbelt, respectively. The insets show their corresponding cross-sectional SEM images. e–g) The HR-TEM images of the interface between the core and shell layers, the core portion and the shell portion, respectively.

detailed characterization such as energy dispersive spectroscopy, X-ray diffraction, and selected area electron diffraction has been reported in our previous study.[30]

The growth mechanism of the highly crystallized ZnO–Ga_2O_3 heterostructure microwires is proposed here based on the following reactions. Briefly, the carbon thermal reduction and reoxidization reactions of ZnO (reactions 1 and 2) and Ga_2O_3 (reactions 3 and 4) result in the formation of ZnO microwires and Ga_2O_3 microbelts, respectively. The mixed CO/CO_2 vapors are generated in the carbon-thermal reduction reactions (reactions 1 and 3), and the oxygen source comes from the residual oxygen in the furnace chamber[31–33]

$$\mathrm{ZnO}(s) + \mathrm{C}(s) \rightarrow \mathrm{Zn}(v) + \mathrm{CO/CO_2}(v) \quad (1)$$

$$\mathrm{Zn}(v) + \mathrm{O_2}(v) \rightarrow \mathrm{ZnO}(s) \quad (2)$$

$$\mathrm{Ga_2O_3}(s) + \mathrm{C}(s) \rightarrow \mathrm{Ga}(v) + \mathrm{CO/CO_2}(v) \quad (3)$$

$$\mathrm{Ga}(v) + \mathrm{O_2}(v) \rightarrow \mathrm{Ga_2O_3}(s) \quad (4)$$

Because of the different growth threshold temperature of ZnO (900 °C) and Ga_2O_3 (1100 °C), the synthesis of ZnO–Ga_2O_3 heterostructure could be designed in one temperature-rise continuous reaction process.[34–38] The one-step CVD growth process of the ZnO–Ga_2O_3 heterostructure microwires is schematically illustrated in **Figure 2**. During the temperature-rising process, the Zn vapors first formed at about 900 °C (reaction 1), and then they were adsorbed on the Si substrate with ZnO film as the seed layer to be reoxidized to form new-born ZnO according to reaction 2. Reactions 1 and 2 were the dominant reactions to grow ZnO microwires at the first step (Figure 2a). Upon the consumption of Zn vapors and the increase of temperature to about 1000 °C, the ZnO microwires growth was accomplished (Figure 2b). Then the Ga vapors began to appear following reaction 3. With temperature increasing to 1100 °C, more Ga vapors started to adhere to the ZnO microwires and were reoxidized to form Ga_2O_3 (reaction 4). Reactions 3 and 4 were the dominant reactions to form the Ga_2O_3 shells (Figure 2c). Finally, as the decreasing of the Ga vapors, the ZnO–Ga_2O_3 heterostructure microwire gradually formed on the Si substrate with the temperature keeping at 1200 °C as shown in Figure 2d. This one-step vapor-solid progress method is the key to the formation of the highly crystallized ZnO–Ga_2O_3 heterostructure microwires.

An individual ZnO–Ga_2O_3 heterostructure microwire was selected to construct the photodetector device with In or Ti/Au as the electrodes for ZnO and Ga_2O_3, as shown in the schematic diagram (**Figure 3**a). The dark currents of the heterostructure device are shown in Figure 3b (blue line), which presents an off-state at the reverse bias and an on-state at the forward bias corresponding to the typical single junction rectifying property. The photocurrents under 254 nm light illumination (power density of 1.67 mW cm^{-2}) are shown in Figure 3b (red line), which are two orders larger than the dark currents under the reverse bias while under the forward bias are almost unchanged. It indicates that the heterojunction device is a typical photovoltaic detector. Interestingly, the dramatic difference between the photocurrent and the dark current at 0 V bias demonstrates excellent self-powered photoresponse. The capacitance–voltage (*C*–*V*) curve of the device at the reverse bias is shown in Figure S3 (Supporting Information), which verifies the existence of the junction in this self-powered device, and its capacitance is estimated to be about 13 pF under 0 V. The current–volatge (*I*–*V*) curves of the ZnO microwire metal-semiconductor-metal (MSM) structure with In electrodes are shown in Figure 3c, and the schematic diagram of the MSM structure device is shown in the inset. The linear characteristic of the *I*–*V* curve under dark indicates Ohmic contacts between ZnO and In electrodes, and the resistance of ZnO is relatively low (≈kΩ). No obvious photoresponse is detected under 254 nm light illumination (red line). The linear *I*–*V* curves of the Ga_2O_3 microbelt MSM structure with Ti/Au electrodes are shown in Figure 3d, and the schematic diagram of the MSM structure device is shown in the inset. The linear characteristic under dark also indicates Ohmic contacts between Ga_2O_3 and Ti/Au electrodes, and the resistance of Ga_2O_3 is very high (≈TΩ). The *I*–*V* characteristic under 254 nm light illumination (red line), shows a small increase compared with that under dark (blue line). The ohmic contacts feature from the two MSM structure devices indicates that the rectifying property is only on account of

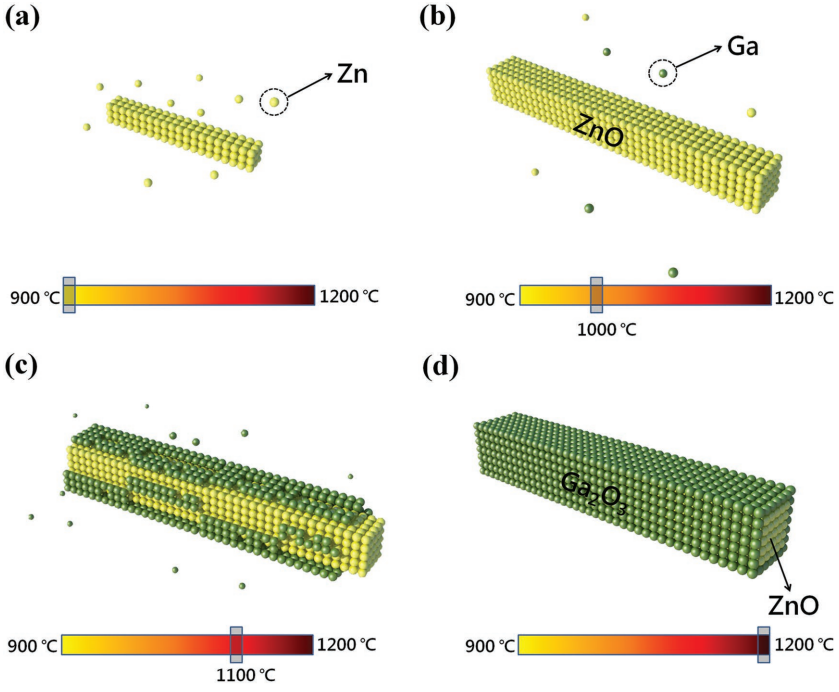

Figure 2. The schematic diagram of the growth process of ZnO–Ga_2O_3 core–shell microwire at a) 900 °C, b) 1000 °C, c) 1100 °C, and d) 1200 °C.

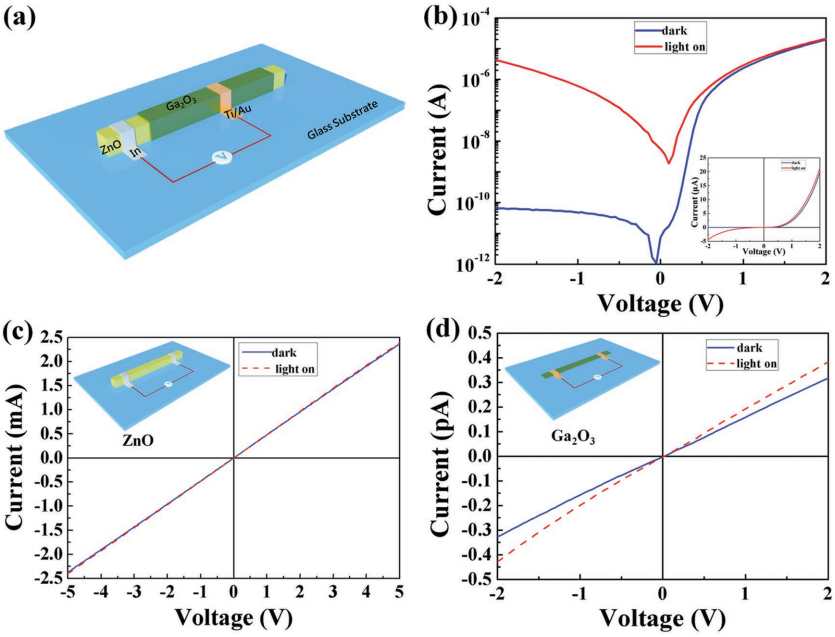

Figure 3. a) The schematic diagram of the heterojunction photodetector device. b) The *I–V* characteristics in a log coordinate of the photodetector under dark (blue line) and illumination with 254 nm light with a power density of 1.67 mW cm^{-2} (red line). The corresponding *I–V* characteristics in a linear coordinate is shown in the inset. c,d) The *I–V* characteristics of the ZnO microwire MSM structure device and the Ga_2O_3 microbelt MSM structure device, respectively.

the heterojunction between ZnO and Ga_2O_3 and the response upon light-on is also due to the presence of the heterojunction.

The photocurrent of the device at 0 V under different wavelengths of the light is shown in **Figure 4**a, which demonstrates that the device can be used as a self-powered photodetector. The maximum photocurrent is located at 257 nm and the photocurrent under solar-blind radiation (<280 nm) is much larger than that under UVB (280–320 nm) and UVA (320–400 nm) radiation. The corresponding optical powder density of the different wavelengths of the light is shown in Figure 4b. The responsivity (R_λ) is an important parameter of a photodetector to estimate a device sensitivity. The responsivity of the photodetector can be calculated by the equation $R_\lambda = (I_\lambda - I_d)/P_\lambda S$, where I_λ is the photocurrent, I_d is the dark current, P_λ is the light intensity, and S is the effective illuminated area.[28] The wavelength dependent photoresponsivity of the device under 0 V can be directly calculated and the results are shown in Figure 4c. The maximum responsivity is 9.7 mA W^{-1} at the wavelength of 251 nm corresponding to the band gap of Ga_2O_3 (4.9 eV), which imply that the photodetector presents a high detectivity to the weak solar-blind signals. A sharp cutoff wavelength defined as the ratio between the maximum and the natural constant ($e \approx 2.718$) is located at 266 nm (<280 nm) as shown in Figure 4c, indicating that the self-powered photodetector is a solar-blind photodetector. It is worthy noting that the cut-off wavelength of 266 nm is located in the solar blind range that causes an excellent solar-blind detectivity. The UV/visible rejection ratio ($R_{251\ nm}/R_{400\ nm}$) of the self-powered solar-blind photodetector is about 6.9×10^2 (Figure 4d), which presents high spectral selectivity of the solar-blind UV region. The rejection ratio ($R_{251\ nm}/R_{280\ nm}$) is 10.5, which indicates that the device can effectively detect the solar-blind radiation signal.[39] The detectivity (D^*) is one of the key figure-of-merits of a photodetector, which usually describes the smallest detectable signals. The detectivity of the photodetector can be determined by $D^* = R_\lambda/(2qJ_d)^{1/2}$, where R is the responsivity of the photodector, q is the elemental charge, and J_d is the dark current density.[40] The calculation value of device's detectivity reaches up to 2.58×10^{12} cm $Hz^{1/2}$ W^{-1} (Jones) at a small bias (−0.1 V), which shows high capability to detect the signal from the noise.

The response time of the device under 0 V bias was measured under the excitation of the 266 nm pulse laser and the results are shown in **Figure 5**a. The rise time from 10% to 90% is ≈100 µs and the decay time from 90% to 10% is ≈900 µs,[41] which is much shorter than that of previous photoconductive type Ga_2O_3 photodetectors (approximately

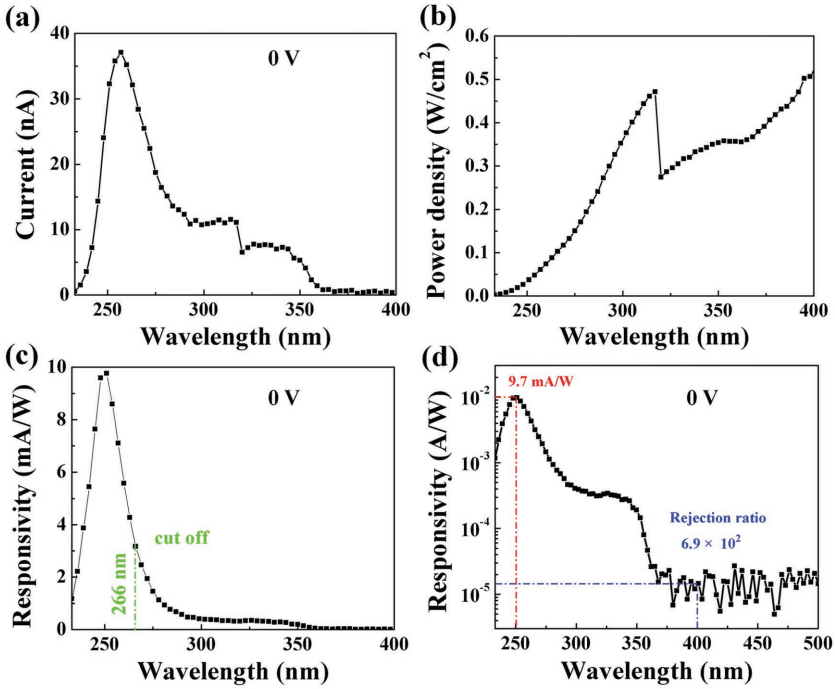

Figure 4. a) The photocurrent of the device at 0 V under different wavelengths of the light. b) The optical powder density of the different wavelengths of the light. c) The photoresponse spectrum of the device at 0 V and d) its spectrum in a log coordinate.

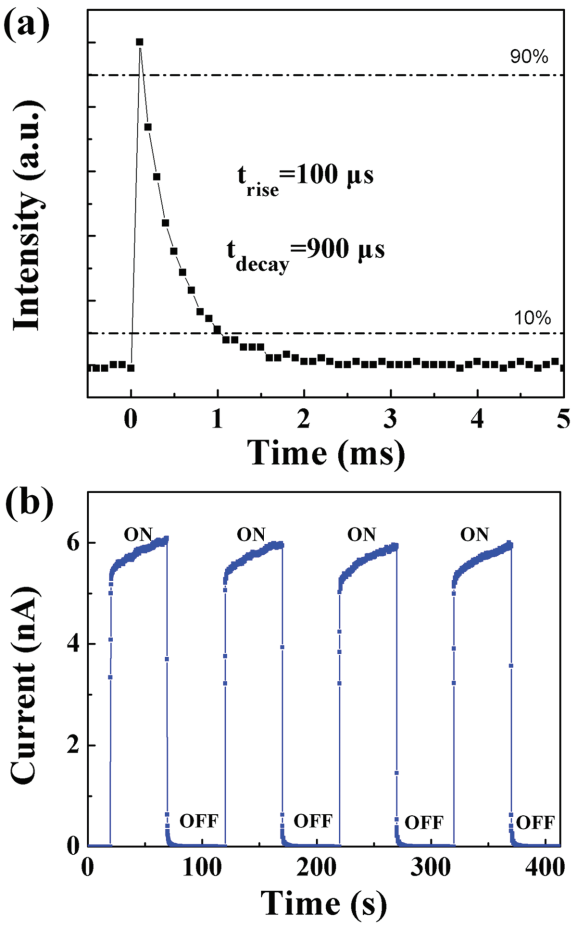

Figure 5. a) The time response under the excitation of 266 nm pulse laser at 0 V. b) The time response characteristics of the "on" and "off" states under the 254 nm light illumination with 1.67 mW cm^{-2} at 0 V.

in seconds). To evaluate the repeatability property of the self-powered photodetector, the time-dependent photocurrent of the device was measured with on/off switching of 254 nm UV light (1.67 mW cm^{-2}) under a working voltage of 0 V (Figure 5b). The dynamic response of the photodetector presents good stability and reproducibility without any external power supply.

The comparison between the ZnO–Ga_2O_3 heterojunction solar-blind photodetector in this study and other reported self-powered solar-blind photodetector devices is listed in **Table 1**. As a self-powered solar-blind photodetector, the ZnO–Ga_2O_3 heterojunction solar-blind photodetector shows a much larger responsivity and detecivity than that of other solar-blind self-powered photodetectors. The rejection ratio of $R_{251\ nm}/R_{400\ nm}$ and $R_{251\ nm}/R_{280\ nm}$ is also comparable to that of previous excellent solar-blind photodetectors. As a photovoltaic detector, the ZnO–Ga_2O_3 heterojunction solar-blind photodetector also shows a fast response speed. In addition, comparing with other UVA self-powered photodetectors, our device shows more desirable responsivity and excellent wavelength selectivity.

By contrast, the wavelength dependent photoresponsivity of the device under −2 V bias is shown in **Figure 6**a. The responsivity peak is centered at 251 nm which is the same as that under 0 V, and the responsivity is as high as 11.1 A W^{-1} at 251 nm. The cutoff wavelength is also at 266 nm (<280 nm). The UV/visible rejection ratio ($R_{254\ nm}/R_{400\ nm}$) is about 1.2×10^3 as shown in the inset of Figure 6b. Compared with wavelength dependent photoresponsivity of the device under 0 V, apart from the response peak located at 251 nm, another response peak is found at around 350 nm under zero bias. It can be ascribed to the response signal of ZnO due to the photons (wavelength > 251 nm) penetrating the Ga_2O_3 layer and being absorbed by ZnO. However, thanks to the conductance band offset and built in electric fields, the photon-generated electrons will be effectively blocked and then recombine with holes, and the corresponding response signal from ZnO side is rather weak and can be eliminated under reverse bias. The response time of the device under −2 V bias is shown in Figure 6c. The rise time from 10% to 90% is ≈100 µs and the decay time from 90% to 10% is ≈600 µs, which is slightly faster than those under 0 V owing to the strengthened built in electric field. The time-resolved photocurrent of the device under −2 V with the illumination of 254 nm UV light with 1.67 mW cm^{-2} is shown in Figure 6d, which also shows a stable and reproducible response. The above results imply that the wavelength dependent photoresponsivity and response speed of this heterojunction under 0 V is comparable to those under reverse bias.

In contrast to this heterojunction photodetector, a back-to-back junction photodetector was further fabricated, and the

Table 1. The characteristic parameters of the ZnO–Ga_2O_3 heterojunction solar-blind photodetector and other heterojunction self-powered solar-blind photodetector devices in the literature.

Photodetector	Wavelength of detection	Responsivity [mA W^{-1}]	$R_{peak}/R_{400\ nm}$ rejection ratio	$R_{peak}/R_{280\ nm}$ rejection ratio	Rise time	Decay time	Detectivity [Jones]	Ref.
Au/Ga_2O_3	258 nm (UVC)	0.01	38	11	1 µs	100 µs	–	[25]
Ga_2O_3/NSTO	254 nm (UVC)	2.6	–	–	0.21 s	0.07 s	–	[42]
Polyaniline/MgZnO	250 nm (UVC)	0.16	≈10^4	5	<0.3 s	<0.3 s	1.5×10^{11}	[43]
Hierarchical $ZnGa_2O_4$	254 nm (UVC)	–	–	–	0.2 s	0.3 s	–	[44]
CuSCN/ZnO	350 nm (UVA)	7.5	100	–	500 ns	6.7 µs	–	[45]
p-GaN/ZnO	358 nm (UVA)	0.65	≈10	–	–	–	–	[46]
ZnO nanoflakes	365 nm (UVA)	2.65	–	–	23 ms	26 ms	5.25×10^{10}	[47]
ZnO/Ga_2O_3	251 nm (UVC)	9.7	6.9×10^2	10.5	100 µs	900 µs	6.29×10^{12}	This work

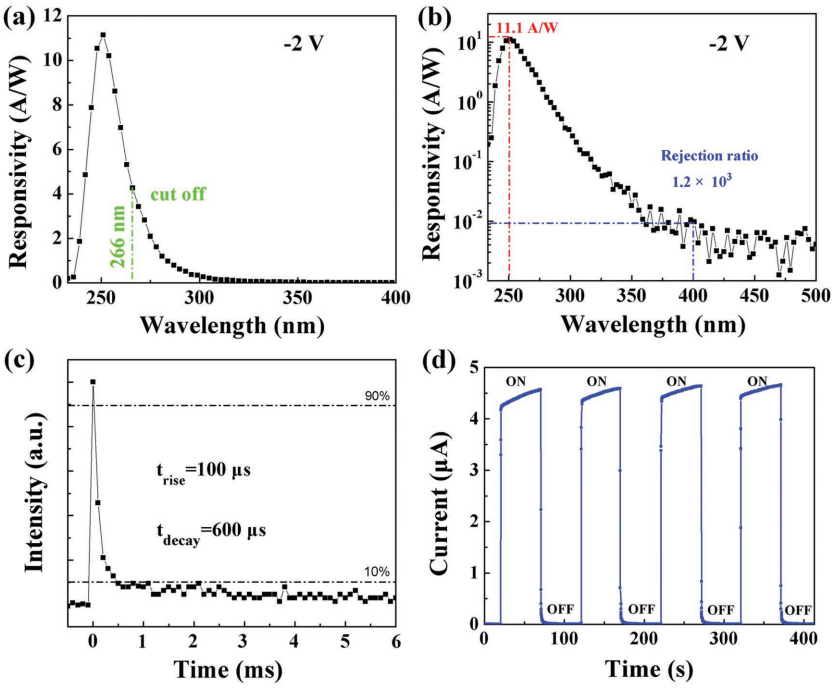

Figure 6. a) The photoresponse spectrum of the device at −2 V and b) its spectrum in a log coordinate. c) The time response under the excitation of 266 nm pulse laser at −2 V d) The time response characteristics of the "on" and "off" states under the 254 nm light illumination with 1.67 mW cm^{-2} at −2 V.

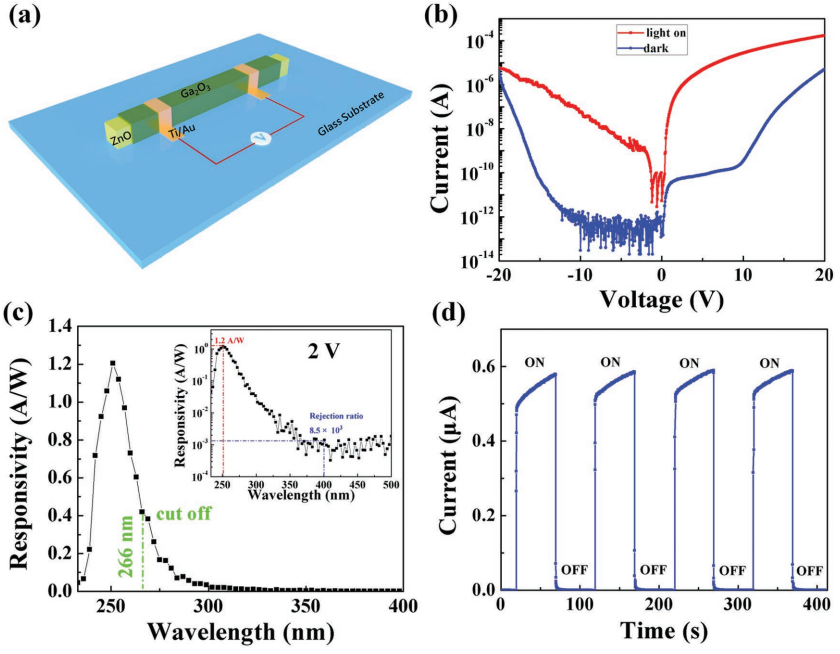

Figure 7. a) The schematic diagram of the back-to-back junction photodetector device. b) The *I*–*V* characteristics in a log coordinate under dark (blue line) and illumination with 254 nm light of 1.67 mW cm^{-2} conditions (red line). c) The photoresponse spectrum of the back-to-back junction device at 2 V. The inset is photoresponse spectrum in a log coordinate. d) The time response characteristics of the "on" and "off" states of the back-to-back junction device under the 254 nm light illumination with 1.67 mW cm^{-2} at 2 V.

schematic diagram is shown in **Figure 7**a. When both two electrodes are contacted with the shell, as the resistance of the core is much larger than that of the shell, the device forms a back-to-back junction device. When the electrodes are on the two ends of ZnO–Ga_2O_3 core–shell microwire as shown in Figure S4a (Supporting Information), where the electrodes both contacting with the core and shell, the *I*–*V* curve shows linear and low resistance (Figure S4b, Supporting Information), which demonstrates that the currents prior go through the low resistance core layer. The *I*–*V* curve of the back-to-back junction device under dark (blue line in Figure 7b) shows an off state under the reverse and forward biases. The photocurrents of the back-to-back junction device under the 254 nm light illumination are much larger than the dark currents whether under the reverse or forward biases (red line in Figure 7b). The photodetective performance of the back-to-back junction photodetector under 0 V exceeds the limitation of our measurement system, and a bias of 2 V is applied to evaluate the wavelength dependent photoresponsivity of the back-to-back junction photodetector (Figure 7c). The responsivity peak under 2 V is also centered at 251 nm with a maximum value of 1.3 A W^{-1}. The cutoff wavelength of responsivity curve is also at 266 nm (<280 nm) and the UV/visible rejection ratio ($R_{254\ nm}/R_{400\ nm}$) is about 8.5×10^2 as shown in the inset of Figure 7c. It is found that the responsivity of heterojunction photodetector under −2 V is about nine times comparing to that of back-to-back junction photodetector. To reach the responsivity of heterojunction photodetector under −2 V, the back-to-back junction photodetector should use 5 V at the forward bias or 19 V at the reverse bias. The time-resolved photocurrent of back-to-back junction photodetector under 2 V with the illumination of 254 nm UV light is shown in Figure 7d, which also shows a stable and reproducible response. Therefore, compared with the back-to-back junction, the heterojunction photodetector not only can be served as a self-powered device, but also shows superior performance at a low power state.

The energy band diagram is illustrated in **Figure 8**a to well understand the self-powered photodetection formation mechanism of the heterojunction device. To construct the band diagram, the electron affinities (χ) of Ga_2O_3 and ZnO are taken as 2.5 and 4.35 eV, respectively, and the bandgap energy (E_g) of Ga_2O_3 and ZnO are 4.9 and

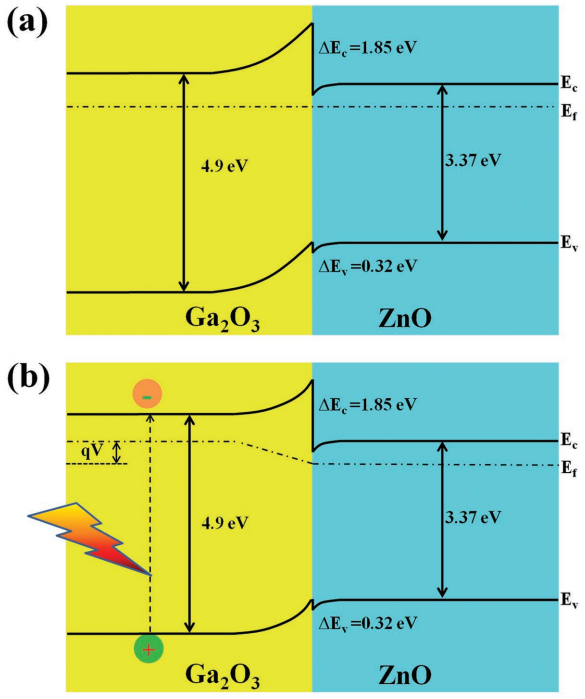

Figure 8. The energy band diagram of the heterojunction device a) under dark state and b) under solar-blind waveband illumination at 0 V.

3.37 eV, respectively. The energetic barriers of electrons (ΔE_c) and holes (ΔE_v) for Ga_2O_3/ZnO are calculated to be 1.85 and 0.32 eV, respectively.[48] When the ZnO and Ga_2O_3 form heterojunction, due to the diffusion movement of electrons, a space charge region is developed at the interface, and then it generates a built-in electric field which keeps the balance between the drift movement and diffusion movement of electrons under 0 V bias.[38] Upon the solar-blind UV radiation as shown in Figure 8b, the photogenerated electron-hole pairs would break the balance and generate a photoinduced voltage. When connecting the positive and the negative electrodes of the device, it would form the current loop driven by the photoinduced voltage, and then the device can act as a self-powered photodetector.[20,47,49,50] As for the back-to-back junction photodetector under light illumination at 0 V, the two reversed photoinduced voltages will be offset, and it is difficult to measure the responsivity under 0 V bias. Thus, no obvious photoresponse can be found from the back-to-back junction device. For the rectification characteristics of the heterojunction photodetector, the device presents on state at forward voltage and off state at reverse voltage. When the solar-blind radiation is applied, the photoinduced current is much larger than the dark current at the reverse bias, and less than or equal to the dark current at forward bias. Hence, the photocurrents are two orders larger than the dark currents under the reverse biases and the currents under the forward biases are seldom changed. And as for the back-to-back junction device, whether at the forward or reverse voltage, it always has one junction staying at on state and the other at off state, leading to much larger photocurrents than the dark currents.

3. Conclusion

In summary, highly crystallized ZnO–Ga_2O_3 heterostructure microwires have been synthesized following a facile one-step CVD method. A solar-blind photodetector has been constructed based on an individual ZnO–Ga_2O_3 heterojunction, and the photodetector can act as a self-powered device, which shows superior performance in solar-blind waveband radiation under zero bias. The responsivity at 251 nm can reach up to 9.7 mA W^{-1} without any power supply with a high UV/visible rejection ratio ($R_{251\ nm}/R_{400\ nm} = 6.9 \times 10^2$), which is much higher than that of the previous self-powered solar-blind photodetectors. In addition, the device also has a fast response speed with the rise time shorter than 100 μs and the decay time of 900 μs under zero bias. The results reported in this paper provide a facile route to constructing self-powered solar-blinded UV photodetectors with high responsivity and thus may lay a solid ground for the future applications of this kind of microstructure heterojunction photodetectors.

4. Experimental Section

Synthesis and Characterization of the ZnO–Ga_2O_3 Core–Shell Heterostructure Microwires: The ZnO–Ga_2O_3 core–shell microwires were synthesized via a simple one-step CVD method, using a mixture of ZnO, Ga_2O_3, and graphite powders (1:0.1:1 in weight ratio) named sample #1 as the reactant source material. The silicon substrate was laid above the source material with about 100 nm ZnO film as the seed layer (deposited via a radio frequency magnetron sputtering method). The furnace was heated to 1000 °C with a speed of 25 °C min^{-1} and then heated to 1200 °C with a speed of 10 °C min^{-1} under a constant flow of (99.99%) Ar (160 sccm) as the protecting gas. After maintaining at 1200 °C for 40 min, the furnace was cooled down to room temperature naturally. The ZnO microwires and Ga_2O_3 microbelts were synthesized following the same way, using a mixture of ZnO and graphite powders (1:1 in weight ratio) named sample #2 and being heated to 1050 °C with a speed of 25 °C min^{-1}, and Ga_2O_3 and graphite powders (1:1 in weight ratio) named sample #3 and being heated to 1200 °C with a speed of 25 °C min^{-1}, respectively. For comparison, the ZnO–Ga_2O_3 core–shell microwires prepared by a two-step CVD method followed the way of synthesizing ZnO microwires as step one and the way of synthesizing Ga_2O_3 microbelts as step two. The morphology of the microstructure was characterized by a field-emission scanning electron microscopy (Hitachi S-4800) and a TEM. HR-TEM was used to determine the crystalline structures of the microwires.

Photodetector Device Construction: To fabricate the photodetector, a single ZnO–Ga_2O_3 core–shell heterostructure microwire was selected and transferred to a glass substrate. In or Ti/Au thin films with 1 mm wide were evaporated to serve as the electrodes for ZnO and Ga_2O_3, respectively. The *I–V* and *C–V* characteristics were measured using a semiconductor device analyzer (Agilent B1500A). The photoresponse curve of the photodetector was measured at room temperature using a photoresponse testing system including a Xe lamp, a monochromator, a chopper, and a lock-in amplifier. The time-resolved response was measured under the excitation of the 266 nm line of a Nd:YAG laser with the pulsed width of 20 μs, and the transient signals were recorded by a Triax 550 spectrograph.

Supporting Information

Supporting Information is available from the Wiley Online Library or from the author.

Acknowledgements

This work was supported by the National Natural Science Foundation of China (Grant Nos. 11674061, 51471051, 61505033, and 11504367), National Postdoctoral Science Foundation of China (Grant No. 2015M580294, 2015M581525), Science and Technology Commission of Shanghai Municipality (Grant No. 15520720700), and Shanghai Shu Guang Project (Grant No. 12SG01), and the Programs for Professor of Special Appointment (Eastern Scholar) at Shanghai Institutions of Higher Learning. Part of this work was carried out in Fudan Nano-fab Laboratory.

Received: January 16, 2017
Revised: February 20, 2017
Published online:

[1] M. Razeghi, A. Rogalski, *J. Appl. Phys.* **1996**, *79*, 7433.
[2] H. Y. Chen, H. Liu, Z. M. Zhang, K. Hu, X. S. Fang, *Adv. Mater.* **2016**, *28*, 403.
[3] L. Li, P. S. Lee, C. Y. Yan, T. Y. Zhai, X. S. Fang, M. Y. Liao, Y. Koide, Y. Bando, D. Golberg, *Adv. Mater.* **2010**, *22*, 5145.
[4] F. Omnes, E. Monroy, E. Munoz, J. L. Reverchon, *Proc. SPIE* **2007**, *6473*, 1.
[5] T. Oshima, T. Okuno, N. Arai, N. Suzuki, H. Hino, S. Fujita, *Jpn. J. Appl. Phys.* **2009**, *48*, 011605.
[6] G. Chen, Z. Y. Xu, H. P. Ding, B. M. Sadler, *Opt. Express* **2009**, *17*, 3929.
[7] D. Walker, V. Kumar, K. Mi, P. Sandvik, P. Kung, X. H. Zhang, M. Razeghi, *Appl. Phys. Lett.* **2000**, *76*, 403.
[8] T. Tut, M. Gokkavas, A. Inal, E. Ozaby, *Appl. Phys. Lett.* **2007**, *90*, 163506.
[9] G. Parish, S. Keller, P. Kozodoy, J. P. Ibbetson, H. Marchand, P. T. Fini, S. B. Fleischer, S. P. Denbarrs, U. K. Mishra, E. J. Tarsa, *Appl. Phys. Lett.* **1999**, *75*, 247.
[10] L. K. Wang, Z. G. Ju, J. Y. Zhang, J. Zheng, D. Z. Shen, B. Yao, D. X. Zhao, Z. Z. Zhang, B. H. Li, C. X. Shan, *Appl. Phys. Lett.* **2009**, *95*, 131113.
[11] M. M. Fan, K. W. Liu, X. Chen, X. Wang, Z. Z. Zhang, B. H. Li, D. Z. Shen, *ACS Appl. Mater. Interfaces* **2015**, *7*, 20600.
[12] Y. Koide, M. Y. Liao, J. Alvarez, *Diamond Relat. Mater.* **2006**, *15*, 1962.
[13] E. V. Gorokhov, A. N. Magunov, V. S. Feshchenko, A. A. Altukhov, *Instrum. Exp. Tech.* **2008**, *51*, 280.
[14] R. Zhou, Z. Zhang, Q. Liu, J. Hu, L. Sang, M. Liao, W. Zhang, *Small* **2014**, *10*, 1848.
[15] L. W. Sang, M. Y. Liao, M. Sumiya, *Sensors* **2013**, *13*, 10482.
[16] Y. Li, T. Tokizono, M. Liao, M. Zhong, Y. Koide, I. Yamada, J. J. Delaunay, *Adv. Funct. Mater.* **2010**, *20*, 3972.
[17] L. Li, E. Auer, M. Liao, X. S. Fang, T. Zhai, U. K. Gautam, A. Lugstein, Y. Koide, Y. Bando, D. Golberg, *Nanoscale* **2011**, *3*, 1120.
[18] W. Feng, X. Wang, J. Zhang, L. Wang, W. Zheng, P. Hu, W. Cao, B. Yang, *J. Mater. Chem. C* **2014**, *2*, 3254.
[19] L. Peng, L. F. Hu, X. S. Fang, *Adv. Funct. Mater.* **2014**, *24*, 2591.
[20] A. A. Hussain, B. Sharma, T. Barman, A. R. Pal, *ACS Appl. Mater. Interfaces* **2016**, *8*, 4258.
[21] L. X. Zheng, F. Teng, Z. M. Zhang, B. Zhao, X. S. Fang, *J. Mater. Chem. C* **2016**, *4*, 10032.
[22] Z. L. Wang, J. H. Song, *Science* **2006**, *312*, 242.
[23] Y. Yang, W. Guo, J. Qi, J. Zhao, Y. Zhang, *Appl. Phys. Lett.* **2010**, *97*, 223113.
[24] Q. Hong, Y. Cao, J. Xu, H. Lu, J. He, J. L. Sun, *ACS Appl. Mater. Interfaces* **2014**, *6*, 20887.
[25] X. Chen, K. Liu, Z. Zhang, C. Wang, B. Li, H. Zhao, D. Zhao, D. Shen, *ACS Appl. Mater. Interfaces* **2016**, *8*, 4185.
[26] C. L. Hsu, Y. C. Lu, *Nanoscale* **2012**, *4*, 5710.
[27] S. Nakagomi, T. Momo, S. Takahashi, Y. Kokubun, *Appl. Phys. Lett.* **2013**, *103*, 072105.
[28] W. Y. Weng, T. J. Hsueh, S. J. Chang, G. J. Huang, H. T. Hsueh, *IEEE Sens. J.* **2011**, *11*, 999.
[29] K. Chang, J. Wu, *J. Phys. Chem. B* **2005**, *109*, 13572.
[30] B. Zhao, F. Wang, H. Y. Chen, Y. Wang, M. M. Jiang, X. S. Fang, D. X. Zhao, *Nano Lett.* **2015**, *15*, 3988.
[31] G. W. Cong, H. Y. Wei, P. F. Zhang, W. Q. Peng, J. J. Wu, X. L. Liu, C. M. Jiao, W. G. Hu, Q. S. Zhu, Z. G. Wang, *Appl. Phys. Lett.* **2005**, *87*, 231903.
[32] C. Yan, P. S. Lee, *J. Phys. Chem. C* **2009**, *113*, 14135.
[33] X. Duan, G. Chen, C. Li, Y. Yin, W. Jin, L. Guo, H. Ye, Y. Zhu, Y. Wu, *Nanotechnology* **2016**, *27*, 295601.
[34] J. G. Wen, J. Y. Lao, D. Z. Wang, T. M. Kyaw, Y. L. Foo, Z. F. Ren, *Chem. Phys. Lett.* **2003**, *372*, 717.
[35] C. Jin, S. Park, H. Kim, C. Lee, *Sens. Actuators, B* **2012**, *161*, 223.
[36] Y. Huang, Y. Zhang, J. He, Y. Dai, Y. Gu, Z. Ji, C. Zhou, *Ceram. Int.* **2006**, *32*, 561.
[37] F. Fang, D. X. Zhao, B. H. Li, Z. Z. Zhang, J. Y. Zhang, D. Z. Shen, *Appl. Phys. Lett.* **2008**, *93*, 233115.
[38] M. P. Chang, M. H. Chiang, W. T. Lin, C. T. Lee, *Mater. Lett.* **2011**, *65*, 1473.
[39] L. Su, Y. Zhu, D. Yong, M. Chen, X. Ji, Y. Su, X. Gui, B. Pan, R. Xiang, Z. Tang, *ACS Appl. Mater. Interfaces* **2014**, *6*, 14152.
[40] X. Gong, M. Tong, Y. Xia, W. Cai, J. S. Moon, Y. Cao, G. Yu, C. Shieh, B. Nilsson, A. J. Heeger, *Science* **2009**, *325*, 1665.
[41] K. Hu, H. Y. Chen, M. M. Jiang, F. Teng, L. X. Zheng, X. S. Fang, *Adv. Funct. Mater.* **2016**, *26*, 6441.
[42] D. Guo, H. Liu, P. Li, Z. Wu, S. Wang, C. Cui, C. Li, W. Tang, *ACS Appl. Mater. Interfaces* **2017**, *9*, 1619.
[43] H. Y. Chen, P. P. Yu, Z. M. Zhang, F. Teng, L. X. Zheng, K. Hu, X. S. Fang, *Small* **2016**, *42*, 5809.
[44] Y. Teng, L. X. Song, W. Liu, Z. Y. Xu, Q. S. Wang, M. M. Ruan, *J. Mater. Chem. C* **2016**, *4*, 3113.
[45] S. M. Hatch, J. Briscoe, S. Dunn, *Adv. Mater.* **2013**, *25*, 867.
[46] L. Su, Q. Zhang, T. Wu, M. Chen, Y. Su, Y. Zhu, R. Xiang, X. Gui, Z. Tang, *Appl. Phys. Lett.* **2014**, *106*, 072106.
[47] B. D. Boruah, A. Misra, *ACS Appl. Mater. Interfaces* **2016**, *8*, 18182.
[48] L. Zhang, Q. Li, L. Shang, Z. Zhang, R. Huang, F. Zhao, *J. Phys. D: Appl. Phys.* **2012**, *45*, 486103.
[49] L. X. Zheng, K. Hu, F. Teng, X. S. Fang, *Small* **2017**, *13*, 1602448.
[50] S. M. Sze, K. K. Ng, *Physics of Semiconductor Devices*, John Wiley & Sons, Hoboken, NJ **2006**.